CHAPTER 14

METHOD OF FUNDAMENTAL SOLUTIONS FOR FULLY NONLINEAR WATER WAVES

D. L.Young[1] Nan-Jing Wu[2] and Ting-Kuei Tsay[3]

[1]Professor, Department of Civil Engineering and Hydrotech Research Institute,
[2]Ph.D. Candidate, Department of Civil Engineering,
[3]Professor, Department of Civil Engineering,
National Taiwan University, 1, Sec.4, Roosevelt Rd., Taipei, 106, Taiwan
E-mail: *dlyoung@ntu.edu.tw*

Abstract

A meshless numerical model for fully nonlinear water waves by the method of fundamental solutions is presented in this chapter. An approach of handling the moving free surface boundary is proposed. Using the method of fundamental solutions of the Laplace equation as the radial basis functions and locating the source points outside the computational domain, we solved the problem by collocating only a few boundary points since governing equation is satisfied automatically. Very good agreement is observed for three examples for the heights of a wavemaker; the generation of periodic finite –amplitude steep waves; and modulation of monochromatic waves over a submerged obstacle as comparing with analytical, experimental and other numerical works.

1. Introduction

Nonlinear water waves are of paramount importance to the coastal, offshore and ocean engineering but are very difficult to deal with due to the nature of moving free surfaces and involved nonlinear phenomena.

The study of fully nonlinear water wave problems in general uses either the fully nonlinear potential theory or Euler or Navier-Stokes equations. They are usually handicapped or prohibited by the nonlinear features of the kinematic and dynamic free surface boundary conditions plus the quasi-linear advection effects for the Euler and Navier-Stokes equations. To overcome the difficulty of the moving and nonlinear free surfaces and governing equations, extensive works to simulate the propagation of surface gravity water waves have been carried out analytically or numerically or experimentally over the decades. Analytical and numerical solutions are sought in the fully nonlinear potential theory, while most Euler and Navier-Stokes models have to rely on the numerical schemes or experimental studies. Non-fixed (deforming) meshes are needed for traditional numerical methods; such as finite element method (FEM) or finite difference method (FDM) or finite volume method (FVM) for examples see Glauss,[1] Lo and Young.[2] If one tries to solve the problem by conventionally numerical methods such as mixed Eulerian-Lagrangian (MEL) or arbitrary Lagrangian-Eulerian methods (ALE), an excessive number of nodes (moving and fixed) and a huge size of matrix usually accompany with the formulation. Besides, these mesh-based methods will encounter the over-distorted mesh and re-meshing problems during the simulation of water wave evolutions.

Another popular numerical scheme to simulate the nonlinear water waves is the boundary element method (BEM), or named as boundary integral equation method (BIEM). Time-domain boundary element method has been employed for its applicability to compute steep water wave propagation since nonlinear free surface conditions were fully incorporated (Longuet-Higgins and Cokelet;[3] Issacson;[4] Dommermuth and Yue;[5] Grilli et al;[6] Cooker et al;[7] Ohyama and Nadaoka;[8] Grilli et al[9] Particle trajectories and the nonlinear boundary conditions on the free surface can be predicted by the MEL or ALE time marching scheme through the numerical integration in the time domain. The velocity

potential of linear boundary value problem can then be solved directly at the further time step. The review paper of Tsai and Yue[10] explained the MEL approach in detail. Lo and Young [2] work concentrated on the ALE method. Dual BEM has also been introduced to simulate the degenerated linear water wave problems in wave-structure interaction by Chen et al.[11, 12] As BEM is based on solving integral equations, numerical integration along the boundaries is always inevitable. Evaluating these integrals is a tedious and non-economic task since there are singularities on the boundaries, either fixed or moving ones. Furthermore, BEM produces full dense matrices, which is time consuming when solving the linear algebraic system, although BEM is a mesh-reduction and dimension-reduction mesh-based method. Though the dense matrices can be efficiently compressed to some sparse ones and the computation may be speeded up by some means of approximation such as fast multipole method: Rokhlin,[13] panel clustering: Hackbusch and Nowak[14] or wavelet compression: Beylkin et al,[15] the need of computing tedious singular integrals still remains in BEM with some difficulties for implementing free surface water wave problems. Beck, Schultz and their coworkers: Cao et al;[16,17] Celebi and Beck;[18] Scorpio and Beck,[19] and Young et al[20] alternatively proposed an approach by moving the singularities away from the boundaries and outside the computational domain to desingularize the integral equations. The surface integrals can be evaluated by simpler techniques as a result of the desingularization, thus efficiently reducing the computational time. The approach has been successfully applied[16–19] to simulate both steady and time-dependent water wave problems. However mesh generation and connectivity and numerical integration are still imperative in this desingularized BEM scheme as comparing to the present proposed meshless scheme such as the method of fundamental solutions (MFS).

An innovative class of methods has appeared in the past decade, which attempts to overcome the requirement of computational grids or meshes

of mesh-based methods. These schemes have several names, such as meshless, mesh-free, grid-free, element-free, mesh-reduction, particle or finite point methods, including the Galerkin and collocation methods. All of them share the common characteristics of no need of mesh and associated explicit connectivity information, which is built by the method in a process designated by the users. The connectivity includes node-to-node distances, azimuths and the sequential relations among these nodes. The basic idea of meshless method is the construction of radial basis functions (RBFs) that only states the relationship between the two-point distances which are very easily extended to the multi-dimensional problems. The RBFs were first developed for interpolating scattered data: Hardy;[21] Franke,[22] and later became a kind of artificial neural network kernels: Moody and Darken.[23] The applications of the concepts of RBFs to solve partial differential equations (PDEs) have been introduced for years: Kansa.[24] Many meshless methods have been reported in the recent literature, such as element free Galerkin method: Belytschko et al[25], diffusion element method: Nayroles at el[26], reproducing kernel particle method: Liu et al[27], smoothed particle hydrodynamics (SPH) method: Monaghan,[28] particle finite element method: Onate et al,[29] meshless local Petrov-Galerkin (MLPG) method: Atluri;[30] Ma,[31] method of fundamental solutions (MFS) : Kupradze and Aleksidze;[32] Fairweather and Aarageorghis;[33] Wu et al[34] and so on. Among them, the SPH, MLPG and MFS have been widely used to simulate water wave problems. Generally speaking, there are two kinds of meshless methods, namely the domain-type and the boundary-type methods. In the domain-type meshless method, any single RBF does not satisfy the governing equations, and there must be a large number of collocation points in both the computational domain as well as the boundary to obtain a better solution. Thus neither the number of nodes nor the size of matrix is reduced too much, and the advantages of domain meshless approach are just for easy programming and avoiding

the chore of mesh generation. There are many works in the literature on solving fluid dynamics problems with domain-type meshless methods such as: Du;[35-36] Zhou et al;[37] Young et al;[38] Ata and Soulaimani;[39] Ma.[31] On the other hand, in the boundary meshless method in some PDEs (such as Laplace, Helmholtz, etc. for example), one can choose the fundamental solutions of the linear operators to be the RBFs: Golberg and Chen;[40] Young et al,[41] which will automatically satisfy the governing equations except at the centers of RBFs. If all the source points (centers of RBF) are set outside the computational domain, there will be no singularity in the computational domain at all and only collocation on the boundary points is needed to solve the problems. One kind of these meshless methods is named as the method of fundamental solutions (MFS). The idea of MFS is similar to the desingularized BEM, while the difference is that desingularized BEM still needs some numerical integration along boundary meshes (or elements) one by one, but MFS only employs collocation about the boundary points without needing any mesh generation and numerical integration. Therefore the MFS is more simple and efficient than the desingularized BEM to model nonlinear water wave problems.

Among the works of investigation of the nonlinear water wave problems governed by the fully nonlinear potential theory, perturbation techniques to linearize the system to become linear or higher order theories are usually employed to deal with the moving and fully nonlinear free surface boundary conditions. After perturbation work is undertaken, the difficulty of free surface boundary conditions is circumvented by a fixed boundary which becomes weakly nonlinear or even linear in the time domain such as: Peregrine;[42] Fenton and Rienecker;[43] West et al;[44] Dommermuth and Yue;[45] Issacson and Cheung;[46] Nwogu;[47] Zhu et al[48] as well as in the frequency domain for example: Massel;[49] Vada;[50] Palm;[51] Sulisz[52]. Perturbation approaches, always accompanying with complicated, prolix and tedious equations and scheme formulations,

might lose some degrees of accuracy and fail to properly treat the fully nonlinear wave problems. Without simplification through perturbation procedure, solving the fully nonlinear water wave problems directly will encounter the severe situation that the boundary at the free surface is moving, nonlinear and not known a *periori*.

For the meshless modeling on the linear and nonlinear water wave problems, Young et al [53] solved the simple linear water wave problem with a semi-infinite domain of normal incident water wave past a submerged breakwater using the hypersingular meshless method (HMM) which is a further improvement of the MFS in selecting the source positions. Wu et al[34, 54] used the MFS to solve the two-dimensional fully nonlinear water wave problems governed by the fully nonlinear potential theory. Ma[33, 55, 56] employed the meshless local Petrov-Galerkin (MLPG) methods to simulate the two-dimensional nonlinear water wave problems for an incompressible and inviscid fluid based on the Euler equations. Hon et al[57] first used the multiquadrics (MQ) method to study the two-dimensional shallow water wave equations and applied to the Hong Kong harbor. They used the partial derivatives of RBFs and scattered collocation points to solve the shallow water equations problems in irregular topographic water bodies. However we are going to limit ourselves in this chapter to review the investigation of fully nonlinear water wave problems governed by the fully nonlinear potential theory using the meshless MFS methods only, since this topic is still in its infancy as far as meshless numerical modeling of linear and nonlinear water waves is concerned.

2. Governing Equations and Boundary Conditions

The problem of a free surface water wave propagating in a flume can be considered as a 2-D hydrodynamic problem for the inviscid, irrotational

and incompressible fluids with free surface boundary. Thus, there exists a velocity potential satisfying the Laplace equation

$$\frac{\partial^2 \phi}{\partial x^2} + \frac{\partial^2 \phi}{\partial z^2} = 0 \tag{1}$$

where $\phi(x,z,t)$ is the velocity potential.

At the free surface, the boundary conditions are specified by the following equations

$$\left.\frac{\partial \phi}{\partial z}\right|_{z=\eta} = \frac{\partial \eta}{\partial t} + \left.\frac{\partial \phi}{\partial x}\right|_{z=\eta} \frac{\partial \eta}{\partial x} \tag{2}$$

$$\left.\frac{\partial \phi}{\partial t}\right|_{z=\eta} = -g\eta - \frac{1}{2}\left.\left(\left(\frac{\partial \phi}{\partial x}\right)^2 + \left(\frac{\partial \phi}{\partial z}\right)^2\right)\right|_{z=\eta} \tag{3}$$

where $\eta(x,t)$ is the free surface displacement. The above two equations are called the kinematic and dynamic free surface boundary conditions (KFSBC and DFSBC), respectively.

At the bottom, the boundary condition is the no flux condition. That is

$$\left.\frac{\partial \phi}{\partial z}\right|_{z=-h} = -\left.\frac{\partial \phi}{\partial x}\right|_{z=-h} \frac{dh}{dx} \tag{4}$$

where $h(x)$ is the water depth.

The boundary condition at the wave generator is

$$\left.\frac{\partial \phi}{\partial x}\right|_{x=\xi} = \frac{\partial \xi}{\partial t} \tag{5}$$

where $\xi(z,t)$ is the displacement of the wave paddle.

The boundary condition at the end of the flume is treated as the radiation boundary condition which means waves are always outgoing. It is shown as:

$$\left.\frac{\partial \phi}{\partial x}\right|_{x=x_r} = -\left.\left(\frac{1}{C}\frac{\partial \phi}{\partial t}\right)\right|_{x=x_r} \tag{6}$$

where C is the wave speed.

Now that we have governing equation and boundary conditions, the problem is well posed and can be solved analytically or numerically.

3. Numerical Implementation - MFS

The numerical solution at each time step is assumed as the linear combination of N radial basis functions. That is

$$\phi(x,z,t) = \sum_{i=1}^{N} \alpha_i(t) q_i(x,z) \tag{7}$$

where $q_i(x,z)$ is the radial basis function (RBF) whose center (also named source point) is at (x_i, z_i), and $\alpha_i(t)$ is its weight or intensity of source. The type of RBF chosen for ϕ in water wave problems can be the fundamental solution of a 2-D Laplacian operator. That is

$$q_i(x,z) = ln(r_i) \tag{8}$$

where $r_i = \sqrt{(x-x_i)^2 + (z-z_i)^2}$ is the distance from any position in the computational domain to that specific source point. The solution form satisfies the governing equation automatically throughout the computational domain if all the RBF centers are chosen outside the computational domain. From this point, we can discretize the time domain by using the symbol (n) to denote the n-th time step. The solution can be obtained by solving $\alpha_i^{(n)}$ from the matrix collocated from the boundary conditions only. At each time step, there are N unknowns ($\alpha_i^{(n)}$, $i = 1, \cdots, N$) to be solved. Thus, N boundary points are needed for the method of collocation. Based on the solution form in Eq. 7, the partial derivatives of the velocity potential are shown as

$$\left(\frac{\partial \phi}{\partial x}\right)^{(n)} = \sum_{i=1}^{N} \alpha_i^{(n)} \frac{\partial q_i}{\partial x} \tag{9}$$

$$\left(\frac{\partial \phi}{\partial z}\right)^{(n)} = \sum_{i=1}^{N} \alpha_i^{(n)} \frac{\partial q_i}{\partial z} \tag{10}$$

Then the collocation of surface boundary points is

$$\sum_{i=1}^{N} \alpha_i^{(n+1)} q_i = \left(\phi \big|_{z=\eta} \right)^{(n+1)} \tag{11}$$

where $\phi^{(n+1)}$ at $z = \eta$ is obtained from the KFSBC and DFSBC. The time marching schemes for the KFSBC of Eq. 2 and DFSBC of Eq. 3 can be obtained from the second-order finite difference in time. That is:

$$\eta^{(n+1)} = \eta^{(n-1)} + 2\Delta t \left(\frac{\partial \phi}{\partial z}\bigg|_{z=\eta} - \frac{\partial \phi}{\partial x}\bigg|_{z=\eta} \frac{\partial \eta}{\partial x} \right)^{(n)} \tag{12}$$

$$\left(\phi \big|_{z=\eta} \right)^{(n+1)} = \left(\phi \big|_{z=\eta} \right)^{(n-1)} - 2\Delta t \left(g\eta + \frac{1}{2}\left(\left(\frac{\partial \phi}{\partial x} \right)^2 + \left(\frac{\partial \phi}{\partial z} \right)^2 \right) \bigg|_{z=\eta} \right)^{(n)} \tag{13}$$

The collocation of bottom boundary points of Eq. 4 and wave paddle boundary points of Eq. 5 are

$$\sum_{i=1}^{N} \alpha_i^{(n+1)} \left(\frac{\partial q_i}{\partial z} + \frac{dh}{dx} \frac{\partial q_i}{\partial x} \right) = 0 \tag{14}$$

$$\sum_{i=1}^{N} \alpha_i^{(n+1)} \frac{\partial q_i}{\partial x} = u_b^{(n+1)} \tag{15}$$

where $u_b^{(n+1)}$ is the known velocity of wave paddle.

Furthermore, the boundary condition at the end of the flume of Eq. 6 can also be applied as

$$\sum_{i=1}^{N} \alpha_i^{(n+1)} \left(q_i + \frac{C\ \Delta t}{2} \frac{\partial q_i}{\partial x} \right) = \phi^{(n)} - \frac{C\ \Delta t}{2} \left(\frac{\partial \phi}{\partial x} \right)^{(n)} \tag{16}$$

Apart from the above description, the gradient of free surface in Eq. 12 is needed for solving the problem. Wu et al[34] proposed the second-order finite difference in space to approximate the gradient of free surface. Boundary points at the free surface were coded in sequence from 1 to N_s, which is the count of surface boundary points. The subscript "*s*" denotes the free surface. The gradient of free surface displacement at any

specific boundary point can be approximated by a second-order finite difference scheme as

$$\left(\frac{\partial \eta}{\partial x}\right)_j^{(n)} = \begin{cases} \dfrac{-\eta_{j+2}^{(n)} + 4\eta_{j+1}^{(n)} - 3\eta_j^{(n)}}{2\Delta x} & , j = 1 \\ \dfrac{\eta_{j+1}^{(n)} - \eta_{j-1}^{(n)}}{2\Delta x} & , j = 2, \cdots, N_s - 1 \\ \dfrac{\eta_{j-2}^{(n)} - 4\eta_{j-1}^{(n)} + 3\eta_j^{(n)}}{2\Delta x} & , j = N_s \end{cases} \tag{17}$$

Since boundary points on the free surface must be coded in sequence and arranged in equal space, this method still needs meshes on the free surface. To establish a really meshless model, Wu et al[54] adopt another interpolating method of RBF type artificial neural network and choose the Gaussian function to be the RBF to fit the free surface. That is

$$\eta(x,t) = \sum_{i=1}^{N_s} \beta_i(t)\, p_i(x) \tag{18}$$

$$p_i(x) = \exp\left(\frac{-(x-(x_s)_i)^2}{\sigma_i^2}\right) \tag{19}$$

where $p_i(x)$ is the RBF whose center is at $(x_s)_i$, and $\beta_i(t)$ is its weight. Following the above-mentioned discretization in the time domain, $\beta_i(t)$ can be written as $\beta_i^{(n)}$ at the n-th time step. The values of σ_i are the shape parameters denoting the range of influence of these RBFs. The reason for choosing the Gaussian RBFs to fit the free surface displacements is that when solving the weights of these RBFs the matrix will become sparse and banded and can be solved rapidly by iterating solvers, if the values of the σ_i are small. However, as σ_i approach to zero, the Gaussian RBFs perform like the delta functions and the value of $\eta(x,t)$ is always zero except when x is at one of the RBF centers. The value of σ_i should be chosen properly to avoid this kind of singular condition and to solve the problem quickly. According to our

experiences, the value of the shape parameter should be greater than half of nodal spacing to keep off the singularity. As the free surface at the n-th time step $\eta^{(n)}$ is known, the weights $\beta_i^{(n)}$ can be solved from the linear algebraic system, and then the gradient of free surface can be obtained as

$$\left(\frac{\partial \eta}{\partial x}\right)^{(n)} = \sum_{i=1}^{N_s} \beta_i^{(n)} \frac{d}{dx} p_i(x) \tag{20}$$

The procedures of numerical implementation are illustrated as follows:

Step 1: The velocity potential in the entire domain ϕ and the particle displacement at the free surface η are all set equal to zero initially (at $n=-1$ and $n=0$).

Step 2: The positions of collocation points at the wave paddle for the $(n+1)^{th}$ step are updated.

Step 3: The free surface displacement and the velocity potential at the free surface are calculated by Eqs. 12 and 13, respectively. The positions of collocation points at the free surface for the $(n+1)^{th}$ step are then updated.

Step 4: Calculating the partial derivatives of the RBFs at all collocation points, the boundary conditions at the free surface, the bottom and the two ends of the flume are then applied. And the solution of the velocity potential in the entire domain at the $(n+1)^{th}$ step can thus be obtained.

Step 5: The number of time steps proceeded is checked. If the requirement of time steps is not achieved, step 2 for the next time step is then processed.

4. Model Applications

4.1 Wave Heights of a Piston-type Wavemaker

Ursell et al[58] observed and discussed the waves generated by a finite-amplitude harmonically oscillating paddle of a piston-type

wavemaker. The wave heights were less than predicted by the small amplitude wave theory because of the finite-amplitude effects. Ursell et al[58] carried out 20 test runs for small amplitude waves, and 4 test runs for high steep waves. The experimental works were to test the validation of the small-amplitude wave theory and also to find the finite-amplitude effects on the wave characteristics. The wave conditions included the wave period T, water depth h, wave height H, and the wavemaker stroke S. Table 1 lists the wave conditions for high wave-steepness cases. The paddle position of the piston-type wavemaker in the numerical model is a function of time as follows:

$$\xi(t) = -\xi_0 \cos \omega t \tag{21}$$

where ω is the radian frequency and $\xi_0 (= S/2)$ is the amplitude of the harmonically oscillating paddle.

The arrangement of source points and boundary points is shown in Fig.1. Horizontal spacing of adjacent boundary points along the free surface is 0.1 m (about 1/10 ~ 1/13 wave length). The interval of numerical time step is with the order of 1/50 wave period. When simulation time achieves several wave periods, quasi-steady solution nearby the wave paddle can be obtained, and then the wave height at each specific position will be calculated by subtracting the lowest water level from the highest during the time interval of one wave period. The wave height distributions near the wave paddle are shown in Fig.2. For short wave cases one can find the evanescent waves are significant nearby the wave paddle. Since the actual position of wave gage was not mentioned by Ursell et al[58], we calculate the average wave height in the range of $x = 1.0m \sim 3.0m$ in order to compare with experimental data and the small amplitude wave theory. This distance is far enough to avoid taking the evanescent waves into account in these cases. The comparisons are illustrated in Fig.3. For the case of deep water wave ($h/L > 0.5$), the numerical result matches to the experimental data quite well. While for the other cases, the wave heights generated by present model is slightly

higher than experimental data, but still much lower than predicted by the small amplitude wave theory. This demonstrates that the wave heights by the small amplitude wave theory are generally over predicted. As far as wave heights are concerned, the nonlinearity plays a vital role for the finite-amplitude waves.

Table 1 List of Ursell et al's[58] finite amplitude wave generation conditions

run	T(sec)	S(cm)	h(ft)	$H_{measured}$ (cm)
21	0.79	2.54	2.00	4.77
22	0.85	3.15	1.50	5.25
23	0.95	4.50	1.00	5.47
24	0.96	5.73	0.66	5.14

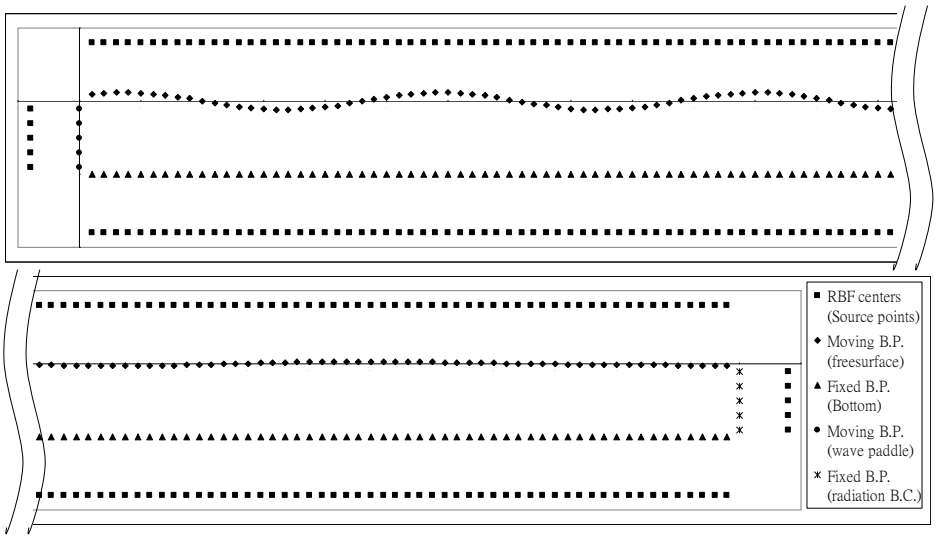

Fig.1 The arrangement of source points and boundary points

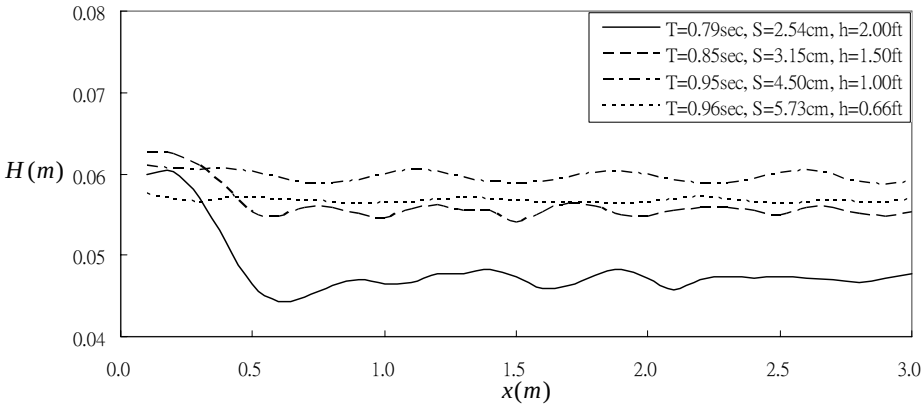

Fig.2 Wave height distributions near the wave paddle

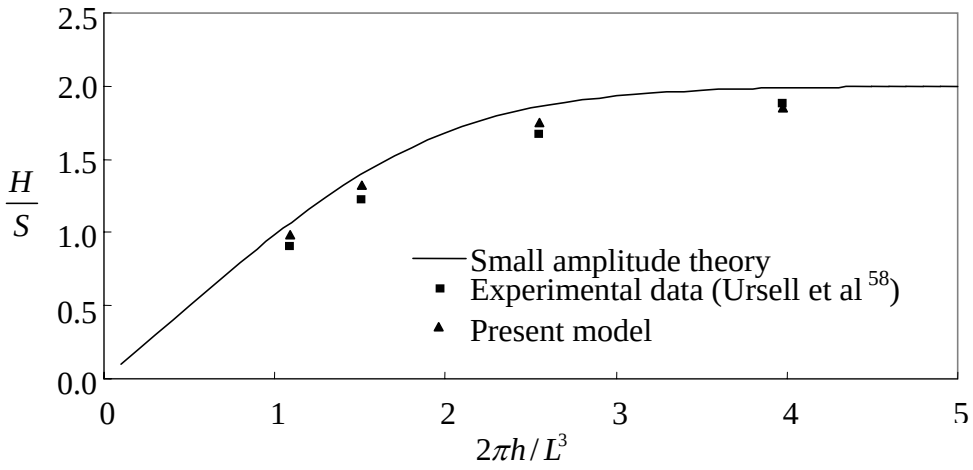

Fig.3 Comparison with the experimental data about the deviation from wave maker theory due to finite wave steepness

4.2 Second Harmonic Wave Components Generated by a High-stroke Wavemaker

As the stroke of the wave paddle of piston-type wavemaker gets higher, the nonlinearity becomes more dominant. While solving the second-order equations for the wave making problem, Madsen[59] found that if the motion of the wave paddle was prescribed as Eq.21, the generated surface profile would have this form

$$\eta = -a\cos(k_p x - \omega\, t) - a_{2p}\cos 2(k_p x - \omega\, t) + a_{2f}\cos(k_f x - 2\omega\, t) \quad (22)$$

where

$$a = \frac{\xi_0 \tanh k_p h}{n_1} \quad (23)$$

$$n_1 = \frac{1}{2}\left(1 + \frac{2k_p h}{\sinh 2k_p h}\right) \tag{24}$$

$$a_{2p} = \frac{k_p a^2}{4}\frac{(2+\cosh 2k_p h)\cosh k_p h}{\sinh^3 k_p h} \tag{25}$$

$$a_{2f} = \frac{a^2 \cosh k_p h}{2h}\left(\frac{3}{4\sinh^2 k_p h} - \frac{n_1}{2}\right)\frac{\tanh k_f h}{n_2} \tag{26}$$

$$n_2 = \frac{1}{2}\left(1 + \frac{2k_f h}{\sinh 2k_f h}\right) \tag{27}$$

In Eqs. 22-27 k_p and k_f denote the wave number of the fundamental wave and the free wave, respectively. The wave numbers can be obtained from the following dispersion relations

$$\omega^2 = g k_p \tanh k_p h \tag{28}$$

$$4\omega^2 = g k_f \tanh k_f h \tag{29}$$

The first term on the right hand side of Eq. 22 is the first-order wave component. The second term represents the Stokes second-order waves traveling at the same speed as the first-order wave. The third term is the second-order free wave, which travels at its own speed.

Madsen[59] performed some experiments to verify the above theories. One of the experiments was conducted in a wave channel with a water depth $h = 38$ cm and a period of the first harmonic $T = 2.75$ sec. The motion of the piston-type wavemaker was taken to be sinusoidal with an amplitude $\xi_0 = 6.1$ cm. This case was numerically simulated by Dong and Huang[60] using a finite-analytic model directly solving the continuity equation and the Navier-Stokes equations. The length of our numerical wave flume is 40 m. A moderate horizontal nodal spacing for simulating nonlinear free surface waves is empirically taken less than 1/20 local wave length. We choose the horizontal spacing of adjacent boundary

points on the free surface to be 0.25 m as a constant, about 1/21 local wave length. For convenience, we also set the horizontal spacing of adjacent boundary points at the flume bottom to be a constant of 0.25 m. The horizontal spacing of source points above the free surface and beneath the bottom boundary is also 0.25 m. There are 324 source points outside the computational domain. We tested our model and found that numerical instability may occur if the offset distance to the sources from the boundary is less than the nodal spacing. The interval of numerical time step is taken to be 0.04 sec. The numerical results of free surface displacement at two stations, x = 4.9 m and 8.7 m, are illustrated in Fig. 4a and Fig. 4b, respectively. The comparisons show that the numerical results coincide with the experimental data and the analytical results as well as the results of the other numerical models. The numerical results of free surface profile at t = 21.8 sec along the wave flume are shown in Fig. 5. Our potential results compared well with those of Dong and Huang[60] although they used the viscous and rotational Navier-Stokes model. From the shape of the wave profile, one can find that the sinusoidally moving wave paddle does generate second-order free waves, which disrupt the permanent wave form. Observations from Figs. 4 and 5 indicate that the inertia force dominates the wave motion and ignoring the viscous effect is a reasonable assertion when solving such kind of water wave problems.

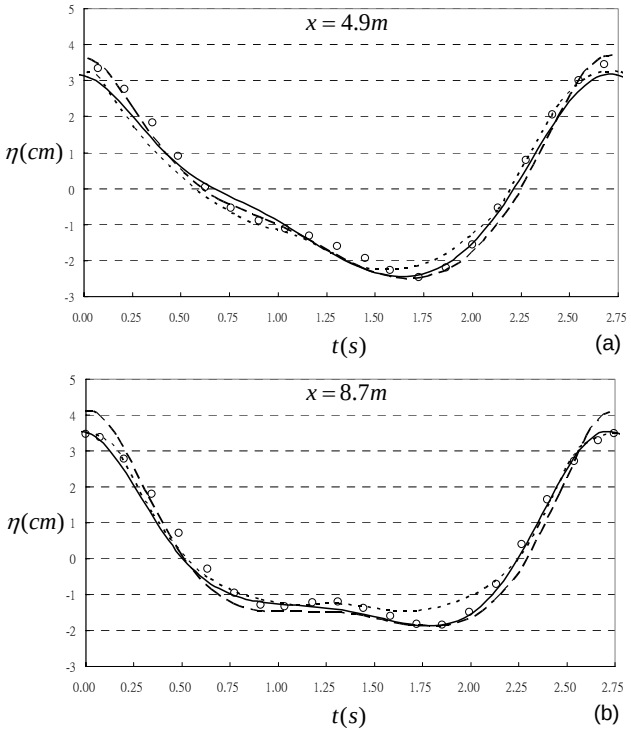

Fig. 4. Comparison between observed, predicted, and numerical surface displacements generated by sinusoidally moving wavemaker: (- - - - -) experimental data (Madsen[59]); (◯) analytical solution from Eq. (22); (— — —) numerical results of Dong and Huang[60]; (——) results from present numerical model

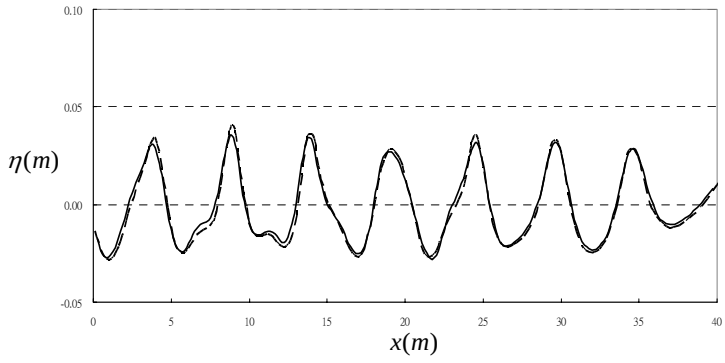

Fig. 5 Numerical results of free surface profile at t = 21.8 s along the wave flume: (— — —) numerical results of Dong and Huang[60]; (——) results from present numerical model

4.3 Monochromatic Waves Passing Over a Submerged Obstacle

Ohyama and Nadaoka[8] developed a BEM model to solve the Laplace equation for the irrotational flow of an inviscid liquid. In order to verify their numerical model and to analyze the modulation of the frequency spectrum for waves traveling over a submerged structure, Ohyama et al[61] carried out near breaking wave generation experiments in a physical wave flume, both monochromatic waves and random ones were generated. The layout of the physical wave flume is shown in Fig. 6. Present model is applied to two monochromatic wave tests, with two different frequencies (0.5 Hz and 0.8 Hz, referred to as the "long" and "short" waves respectively). The wave heights for the two experiments are respectively 0.02 cm and 0.025 cm. Data for comparison were digitized from the paper of Ohyama et al[61] We applied the radiation boundary condition on the slope at the position of 0.15 m water depth in the rear part of the flume. For the long wave test, horizontal spacing of adjacent boundary points in front of the shelf varies from 0.1 m to 0.2 m, about 1/20 local wave length. We set the horizontal spacing above the shelf and in the lee region as a constant of 0.1 m, to obtain fine resolution for strong nonlinear waves. There are 398 source points outside the computational domain. For the short wave test, the boundary points are arranged in a similar regulation, while the horizontal spacing of adjacent boundary points is in the range from 0.08 m to 0.125 m, and the number of source points is 552. We also simulate these cases by arranging the free surface nodes in constant space, with 508 and 634 source points for long and short wave cases respectively. The numerical results of the free surface displacements for long and short monochromatic waves are shown in Figs. 7 and 8, respectively. The comparison shows that present model performs very well as the other experimental or numerical results.
It is worthwhile to observe how the initially sinusoidal wave form evolves as it travels over the obstacle. In the upslope region, saw-toothed shape waves with the slight forward pitch can be observed. On the top of

the shelf, both short and long waves are reminiscent of the soliton formation behind a solitary wave propagating into a shallow depth. In the deepening region, because the higher harmonic free components travel at their own speeds, no permanent wave shape can be formed. One can discover that the evolution of the short waves is less appreciable. This is because the short waves are less obstructed by the seabed than the long waves.

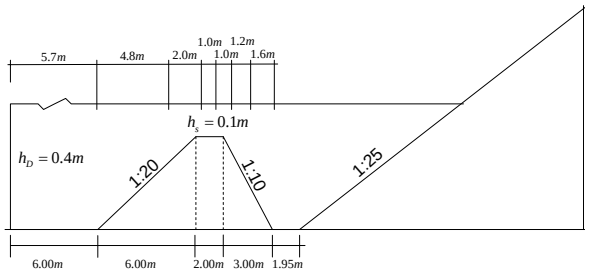

Fig. 6 Wave flume and locations of wave gages (Ohyama et al[61])

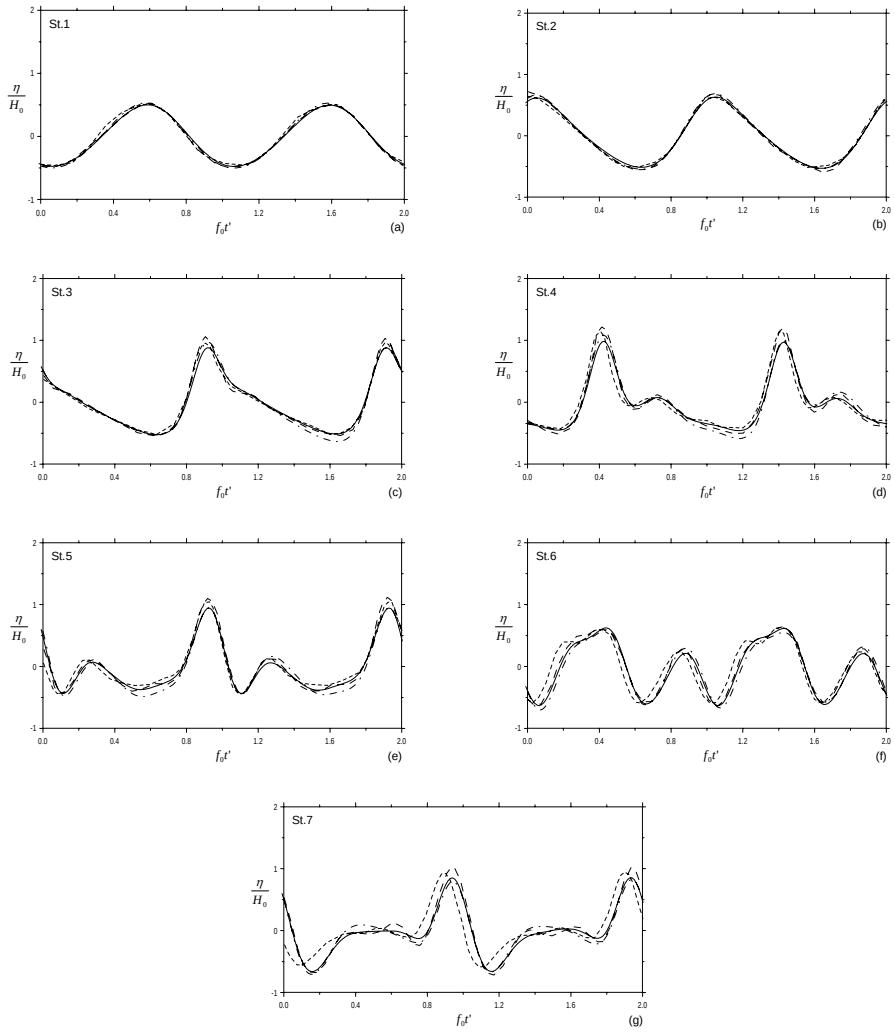

Fig. 7 Free surface displacements for long monochromatic waves at stations 1-7: (- - - - -) experimental data (Ohyama et al[61]); (— — —) numerical results of Ohyama et al;[61] (— · — ·) present results with constant nodal spacing; (——) present results with varying nodal spacing

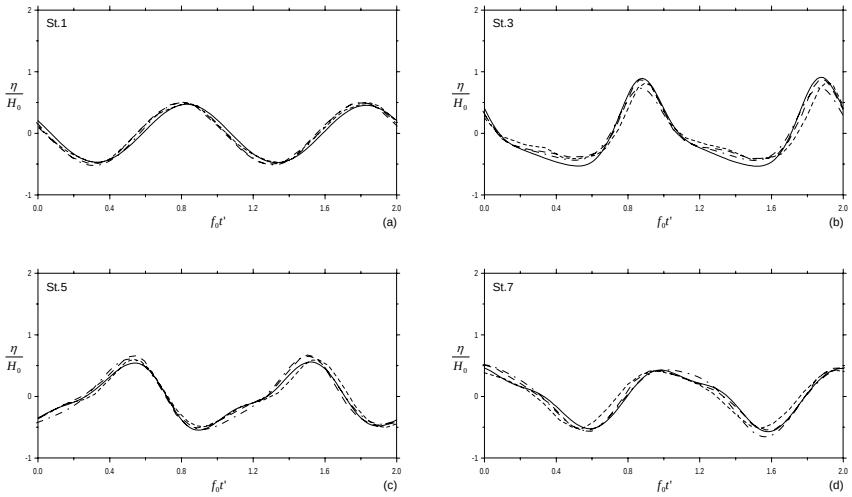

Fig. 8 Free surface displacements for short monochromatic waves at stations 1, 3, 5, and 7: (- - - -.) experimental data (Ohyama et al; [61]) (— — —) numerical results of Ohyama et al; [61] (— · — ·) present results with constant nodal spacing; (———) present results with varying nodal spacing

5. Conclusions

This boundary-type meshless method requiring neither domain nor surface meshing is suitable for solving problems with deforming and/or moving boundaries. In free surface water wave problems, fundamental solution of the Laplace operator is chosen to be the form of the radial basis function so that only collocation points along the boundary are needed. By fitting the free surface displacement with Gaussian radial basis function, a truly meshless model is established. The MFS is an alternative method with neither prolix scheme formulation nor tediously iterating procedures for simulating fully nonlinear free surface gravity water wave problems.

The MFS has been successfully applied to calculate the following three nonlinear water wave problems: 1. Wave heights of a piston-type wavemaker, 2. Second harmonic wave components generated by a high stroke wavemaker, and 3. Monochromatic waves passing over a submerged obstacle. Very good agreement of these three case studies is

observed as comparing with analytical solutions, experimental data and other numerical results. This demonstrates that the MFS is a simple and powerful meshless numerical method to simulate the nonlinear water wave problems.

Acknowledgment

The work presented in this chapter was supported by the National Science Council, Taiwan under the grant number 95-2221-E-002-406. It is greatly appreciated.

References

1. G. Glauss, *Appl. Ocean Res.*, **24**, 147 (2002).
2. D.C. Lo, and D.L.Young, *J. Comput. Phys.*, **195**, 175 (2004).
3. H. S. Longuet-Higgins, and E. D. Cokelet, *Proc. R. Soc. London*, **A350**, 1 (1976).
4. M. Issacson, *J. Fluid Mech.*, **120**, 267 (1982).
5. D. G. Dommermuth, and D. K. P. Yue, *J. Fluid Mech.*, **178**, 195 (1987).
6. S. T. Grilli, J. Skourup, and I. A. Svendsen, *Eng. Anal. Bound. Elem.*, **6**, 97 (1989).
7. M. J. Cooker, D. H. Peregrine, and O.Skovggard, *J. Fluid Mech.*, **215**, 1 (1990).
8. T. Ohyama, and K. Nadaoka, *Fluid Dyn. Res.*, **8**, 231 (1991).
9. S. T. Grilli, P. Guyenne, and F.Dias, *Int. J. Numer. Methods Fluids*, **35**, 829 (2001).
10. W.T. Tsai, and D.K.P.Yue, *Annu. Rev. Fluid Mech*., **28**, 249 (1996).
11. K.H. Chen, J.T. Chen, C.Y. Chou, and C.Y. Yueh, *Eng. Anal. Bound. Elem.*, **20**, 917 (2002).
12. K.H. Chen, J. T. Chen, S.Y. Lin, and Y. T. Lee, *J. Waterw. Port Coast. Ocean En g.-ASCE*, **130**, 179 (2004).
13. V. Rokhlin, *J. Comput. Phys.*, **60**, 187 (1985).
14. W. Hackbusch, and Z.P. Nowak, *Numer. Math.*, **54**, 463 (1989).
15. G. Beylkin, R. Coifman, and V. Rokhlin, *Commun. Pure Appl. Math.*, **44**, 141 (1991).
16. Y. S. Cao, W. W. Schultz, and R. F. Beck, *Int. J. Numer. Methods Fluids*, **12**, 785 (1991).
17. Y.S. Cao, R.F. Beck, and W.W. Schultz, *Int. J. Numer. Methods Fluids*, **17**, 905 (1993).
18. M.S. Celebi, and R. F. Beck, *J. Ship Res.*, **41**, 17 (1997).

19. S.M. Scorpio, and R.F. Beck, *J. Offshore Mech. Arct. Eng. Trans. ASME*, **120**, 71 (1998).
20. D.L. Young, W.S. Hwang, C.C. Tsai, and H.L. Lu, *Eng. Anal. Bound. Elem.*, **29**, 224 (2005).
21. R. L. Hardy, *J. Geophys. Res.*, **76**, 1905 (1971).
22. C. Franke, *Math. Comput.*, **38**, 181 (1982).
23. J. Moody, and C. Darken, *Neural Comput.*, **1**, 281 (1989).
24. J. E. Kansa, *Comput. Math. Appl.*, **19**, 127 (1990).
25. T. Belytschko, Y.Y.Lu, and L. Gu, *Int. J. Numer. Methods Eng.*, **37**, 229 (1994).
26. B. Nayroles, G. Touzot, and P. Villon, *Comput. Mech.*, **10**, 307 (1992).
27. W.K. Liu, Y. Chen, S. Jun, J.S. Chen, T. Belytschko, C. Pan, R.A. Uras, and C.T. Chang, *Arch. Comput. Method Eng.*, **3**, 3 (1996).
28. J.J. Monaghan, *J. Comput. Phys.*, **110**, 399 (1994).
29. E. Onate, S.R. Idelsohn, F. Del. Pin, and R. Aubry, *Int. J. Comput. Methods*, **1**, 267 (2004).
30. S.N. Atluri, *The meshless method (MLPG) for domain & bie discretization*, Tech Science Press, Forsyth, GA, USA (2004).
31. Q. Ma, *J. Comput. Phys.*, **205**, 611 (2005).
32. V.D. Kupradze, and M.A. Aleksidze, *Comp. Maths. Math. Phys.*, **4**, 633 (1964).
33. G. Fairweather, and A. Karageorghis, *Adv. Comput. Math.*, **9**, 69 (1998).
34. N. J. Wu, T. K. Tsay, and D. L. Young, *Int. J. Numer. Methods Fluids*, **50**, 219 (2006).
35. C. J. Du, *J. Hydraul. Eng.-ASCE*, **125**, 621 (1999).
36. C. J. Du, *Comput. Meth. Appl. Mech. Eng.*, **182**, 89 (2000).
37. X. Zhou, Y. C. Hon, and K. F. Cheung, *Eng. Anal. Bound. Elem.*, **28**, 967 (2004).
38. D. L. Young, S. J. Jane, C. Y. Lin, C. L. Chiu, and K. C. Chen, *Eng. Anal. Bound. Elem.*, **28**, 1233 (2004).
39. R. Ata, and A. Soulaimani, *Int. J. Numer. Methods Fluids*, **47**, 139 (2005).
40. M. A. Golberg, and C. S. Chen, *Comput. Mech. publ.*, 103 (1998).
41. D. L. Young, K. H. Chen, and C. W. Lee, *J. Comput. Phys.*, **209**, 290 (2005).
42. D.H. Peregrine, *J. Fluid Mech.*, **27**, 815 (1967).
43. J. D. Fenton, and M. M. Rienecker, *J. Fluid Mech.*, **120**, 267 (1982).
44. B. J. West, K. Brueckner, R.S. Janda, D. Milder, and R. Milton, *J. Geophys. Res. Oceans*, **92**, 11803 (1987).
45. D. G. Dommermuth, and D. K. P. Yue, *J. Fluid Mech.*, **184**, 267 (1987).
46. M. Issacson, and K.F. Cheung, *Appl. Ocean Res.*, **13**, 175 (1991).
47. O. Nwogu, *J. Waterw. Port Coast. Ocean Eng.-ASCE*, **119**, 618 (1993).
48. Q. Zhu, Y. M. Liu, and D. K. P. Yue, *J. Fluid Mech.*, **496**, 213 (2003).
49. S.R. Massel, *Coast. Eng.*, **7**, 357 (1983).
50. T. Vada, *J. Fluid Mech.*, **174**, 23 (1987).
51. E. Palm, *J. Fluid Mech.*, **233**, 49 (1991).

52. W. Sulisz, *J. Waterw. Port Coast. Ocean Eng.-ASCE*, **119**, 160 (1993).
53. D.L.Young, K.H. Chen, J.T. Chen, and J.H. Kao, *CMES-Comp. Model. Eng. Sci.*, **19**, 197 (2007).
54. N.J. Wu, T. K. Tsay, and D.L Young, *J. Waterw. Port Coast. Ocean Eng.-ASCE* (in press).
55. Q. Ma, *CMES-Comp. Model. Eng. Sci*., **9**,103 (2005).
56. Q. Ma, *CMES-Comp. Model. Eng. Sci*., **18**, 223 (2007).
57. Y. C. Hon, K.F. Cheung, X.Z. Mao, and E. J. Kansa, *J. Hydraul. Eng.-ASCE*, **125**, 524 (1999).
58. F. Ursell, R.G. Dean, and Y.S. Yu, *J. Fluid Mech.*, **7**, 33 (1960).
59. O. S. Madsen, *J. Geophys. Res.*, **76**, 8672 (1971).
60. C. M. Dong, and C. J. Huang, *J. Waterw. Port Coast. Ocean Eng.-ASCE*, **130**, 143 (2004).
61. T. Ohyama, S. Beji, K. Nadaoka, and J. A. Battjes, *J. Waterw. Port Coast. Ocean Eng.-ASCE*, **120**, 637 (1994).